AGU PUBLICATIONS

JGR

Journal of Geophysical Research: Oceans

RESEARCH ARTICLE

10.1002/2014JC009994

Key Points:
- The AMOC exhibits high variability on seasonal and shorter time scales
- The intraseasonal and interannual AMOC variability lack a coherent pattern
- The seasonal AMOC variability exhibits two distinct coherent regimes

Correspondence to:
X. Xu,
xxu@coaps.fsu.edu

Citation:
Xu, X., E. P. Chassignet, W. E. Johns, W. J. Schmitz Jr., and E. J. Metzger (2014), Intraseasonal to interannual variability of the Atlantic meridional overturning circulation from eddy-resolving simulations and observations, *J. Geophys. Res. Oceans*, *119*, 5140–5159, doi:10.1002/2014JC009994.

Received 25 MAR 2014
Accepted 21 JUL 2014
Accepted article online 24 JUL 2014
Published online 12 AUG 2014

Intraseasonal to interannual variability of the Atlantic meridional overturning circulation from eddy-resolving simulations and observations

Xiaobiao Xu[1], Eric P. Chassignet[1], William E. Johns[2], William J. Schmitz Jr[3], and E. Joseph Metzger[4]

[1]Center for Ocean-Atmospheric Prediction Studies, Florida State University, Tallahassee, Florida, USA, [2]Rosenstiel School of Marine and Atmospheric Sciences, University of Miami, Miami, Florida, USA, [3]Harte Research Institute, Texas A & M University-Corpus Christi, Corpus Christi, Texas, USA, [4]Oceanography Division, Naval Research Laboratory, Stennis Space Center, Mississippi, USA

Abstract Results from two 1/12° eddy-resolving simulations, together with data-based transport estimates at 26.5°N and 41°N, are used to investigate the temporal variability of the Atlantic meridional overturning circulation (AMOC) during 2004–2012. There is a good agreement between the model and the observation for all components of the AMOC at 26.5°N, whereas the agreement at 41°N is primarily due to the Ekman transport. We found that (1) both observations and model results exhibit higher AMOC variability on seasonal and shorter time scales than on interannual and longer time scales; (2) on intraseasonal and interannual time scales, the AMOC variability is often coherent over a wide latitudinal range, but lacks an overall consistent coherent pattern over the entire North Atlantic; and (3) on seasonal time scales, the AMOC variability exhibits two distinct coherent regimes north and south of 20°N, due to different wind stress variability in the tropics and subtropics. The high AMOC variability south of 20°N in the tropical Atlantic comes primarily from the Ekman transport of the near-surface water, and is modulated to some extent by the transport of the Antarctic Intermediate water below the thermocline. These results highlight the importance of the surface wind in driving the AMOC variability.

1. Introduction

The Atlantic meridional overturning circulation (AMOC hereafter) consists of a net northward flow of warm, saline water in approximately the upper 1 km overlying a net southward flow of cold, fresh water [see *Longworth and Bryden*, 2007; *Richardson*, 2008, for historical review]. Because of its large heat and freshwater transports, and interaction with the atmosphere, the AMOC plays a fundamental role in establishing the mean state and the variability of the climate system. The heat carried in the warm Atlantic water of the upper AMOC limb is known to warm the Northern Hemisphere, and western Europe in particular [*Rhines et al*., 2008]. It may also have triggered the recent rapid melting of the Arctic sea ice [*Serreze et al*., 2007] and Greenland glaciers [*Holland et al*., 2008; *Straneo et al*., 2010]. On a broader scale, fluctuations of the AMOC are often linked to the Atlantic multidecadal oscillation [*Knight et al*., 2005; *Delworth et al*., 2007], the dominant pattern of multidecadal variability in North Atlantic surface temperatures. Because of these profound climate impacts, there is a growing need to quantify, monitor, and understand the spatial structure and temporal variation of the AMOC [*Kuhlbrodt et al*., 2007; *Lozier*, 2010, 2012; *Srokosz et al*., 2012].

Until the establishment of moored instrument arrays and other observation techniques in the past decade, the AMOC and the associated heat transport were typically inferred from transbasin hydrographic section along one latitude, combined with direct measurements of the western boundary currents [*Bryden and Hall*, 1980; *Hall and Bryden*, 1982], or from sections at multiple latitudes in an inverse calculation [*Roemmich*, 1980; *Roemmich and Wunsch*, 1985; *Ganachaud and Wunsch*, 2000; *Lumpkin and Speer*, 2003]. Repeat hydrographic surveys were then used to derive time averages and/or temporal variability at 26°N [*Bryden et al*., 2005], near 48°N [*Koltermann et al*., 1999; *Lorbacher and Koltermann*, 2000; *Lumpkin et al*., 2008], from Cape Farewell to Portugal [*Lherminier et al*., 2010], and at 60°N [*Sarafanov et al*., 2012]. These studies provide averaged estimates of the AMOC transport ranging from 16 to 18.5 Sv, in agreement with the long-term mean formation rate of North Atlantic Deep Water (NADW) as calculated from chlorofluorocarbon inventories,

e.g., 17.2 ± 5.1 Sv in *Smethie and Fine* [2001] and 19.6 ± 3.4 Sv in *LeBel et al.* [2008]. Because of the sparse temporal resolution, the hydrographic data-based studies are not able to provide a consistent picture of the spatial and temporal variability of the AMOC.

The current state-of-the-art approach to measuring the AMOC is to continuously observe the currents and hydrographic fields with a long-term, moored instruments array. Starting in 2004, the joint U.K.–U.S. Rapid Climate Change-MOC program (RAPID, hereafter) have instrumented a complete transbasin section along 26.5°N. Daily mean AMOC transport and the associated vertical structure have been derived from the RAPID data [e.g., *Cunningham et al.*, 2007; *Kanzow et al.*, 2007, 2010; *Johns et al.*, 2008, 2011; *Rayner et al.*, 2011]. The RAPID results show that the AMOC transport is not as steady as previously thought, but rather has a high variability on intraseasonal to seasonal time scales. Some variability on interannual and longer time scales is also observed [*McCarthy et al.*, 2012; *Smeed et al.*, 2014].

In addition to the RAPID array, there are two other significant monitoring efforts that also provide time series of the AMOC transport:

1. At 41°N, the monthly AMOC transports are inferred using a combination of Argo floats and sea-surface height (SSH) data from satellite altimeters [*Willis and Fu*, 2008; *Willis*, 2010; *Hobbs and Willis*, 2012].
2. At 16°N in the tropical North Atlantic, the Meridional OVerturning Experiment (MOVE) array measures the southward flow of NADW within the western basin between the Lesser Antilles Arc and the Mid-Atlantic Ridge [*Kanzow et al.*, 2006, 2008; *Send et al.*, 2011]. The AMOC transport is inferred by assuming that, on interannual and longer time scales, all the southward NADW transport happens in the western basin at this latitude and there is no meridional NADW transport to the east of the MOVE array.

The question as to whether the AMOC variability is coherent across different latitudes has not yet been fully addressed [*Srokosz et al.*, 2012]. *Mielke et al.* [2013] analyzed the seasonal variability observed at 26.5°N and 41°N and compared them to the results from a 1/10° global simulation of *von Storch et al.* [2012]. Their analysis shows that the observed AMOC variability is meridionally covariable between 26.5°N and 41°N on seasonal time scales. They found the same covariability in the model, although the phasing differed from the observations. On longer (decadal) time scales, model studies by *Böning et al.* [2006], *Bingham et al.* [2007], and *Zhang* [2010] show mixed results regarding the latitudinal coherence from the subpolar to the subtropical North Atlantic, but they all exhibit a consistent coherence from the subtropical to the tropical North Atlantic.

In this paper, we further investigate the intraseasonal, seasonal, and interannual variability of the AMOC in the North Atlantic using 1/12° eddy-resolving numerical simulations. After a careful evaluation of the model results in representing the data-based AMOC variability, the latitudinal coherence from the tropical to the subpolar North Atlantic and the structure of the seasonal AMOC variability in the tropical Atlantic are examined. We find that

a. both observations and model results exhibit higher AMOC variability on seasonal and shorter time scales than on interannual and longer time scales;
b. on seasonal time scales, the AMOC variability exhibits two distinct coherent regimes north and south of 20°N, the boundary between the North Atlantic subtropical and tropical gyres; and
c. on intraseasonal and interannual time scales, the AMOC variability is often coherent over a wide latitudinal range, but lacks an overall consistent coherent pattern.

The paper is organized as follows. The observations and model configuration are briefly summarized in section 2. In section 3 we document the AMOC variability in our model via comparison with observations at 26.5°N and 41°N. In section 4 we examine the latitudinal coherence of the AMOC variability on intraseasonal, seasonal, and interannual scales. The vertical structure of the seasonal variability in the tropical North Atlantic is also investigated. A summary and discussion follow in section 5.

2. Observations and Model Configuration

The key observations used in this study are the AMOC transport time series at 26.5°N based on the RAPID data and at 41°N based on Argo and SSH data. The MOVE data at 16°N are not part of this study since they

provide information primarily on long time scales (interannual and longer), which are not the main focus here.

The transbasin AMOC transport at 26.5°N is calculated as the sum of the Florida Current, the Ekman transport, and the mid-ocean transport. The Florida Current is measured by cable [e.g., *Meinen et al*., 2010]. The Ekman transport is estimated from the surface wind fields based on the cross-calibrated multiplatform product (CCMP) [*Atlas et al*., 2011] and the European Center for Medium-range Weather Forecast (ECMWF) reanalysis ERA-interim [*Dee et al*., 2011] when the CCMP is not available. The mid-ocean transport is estimated from the moored instruments array at 26.5°N that measures (1) the velocity of the boundary current within $\sim$ 50 km off the Abaco coast, and (2) dynamic height at both sides of the boundary and both sides of the mid-Atlantic Ridge to infer the transbasin geostrophic transport. An additional constraint of zero net mass transport across the section is used to determine the level-of-no-motion in geostrophic calculations, and to isolate the AMOC from net transport through the Bering Strait [*Bryden and Imawaki*, 2001]. Combining all these components leads to a time series of zonally integrated meridional transport profile, or, when cumulated vertically, the overturning transport streamfunction; see *Cunningham et al*. [2007] and *Kanzow et al*. [2007] for details. The latest time series and mean vertical profile of the overturning streamfunction are shown in Figures 1a and 1b.

Different data and a different approach are used to estimate the AMOC transport at 41°N. Here the displacement of the Argo floats provides an estimate of reference velocity at 1000 m, whereas the Argo floats ascending from 2000 m to the surface measure temperature and salinity profiles. The two are combined to produce geostrophic velocity in the upper 2000 m and high-resolution SSH data from altimeters are used to reduce error induced by mesoscale eddies. Integration of the geostrophic velocity from the surface to the zero meridional velocity (1130 m) together with the Ekman transport from surface wind stress gives the AMOC transport. *Willis* [2010] estimated a mean AMOC transport of 15.5 Sv for 2004–2006, with an uncertainty of about 2 Sv. For the latest time series used in this paper that cover 2002–2012, the mean transport for the same 3 years is 14.5 Sv. The 1 Sv difference is due to the use of different wind products (ERA-interim instead of NCEP/NCAR reanalysis) in estimating the Ekman transport and of a smaller latitudinal interval in estimating the geostrophic current (0.5° instead of 1.5°) (J. Willis and W. Hobbs, personal communication, 2013).

Results from two eddy-resolving numerical simulations using the HYbrid Coordinate Ocean Model (HYCOM) [*Bleck*, 2002; *Chassignet et al*., 2003, 2006] are discussed in this paper. Both simulations (one configured for the North and Equatorial Atlantic, the other global) have a horizontal resolution of 1/12°. Both were initialized using potential temperature and salinity from ocean climatology, the Generalized Digital Environmental Model (GDEM) [*Carnes*, 2009], and were spun-up from rest using climatological atmospheric forcing from the ECMWF reanalysis ERA40 [*Uppala et al*., 2005]. After spin-up (10 years for the global model and 15 years for the Atlantic), the 3 hourly, 0.5° Navy Operational Global Atmospheric Prediction System (NOGAPS) [*Rosmond et al*., 2002] was used to force the global simulation from 2003 to 2012 and the Atlantic simulation from 2004 to 2012.

As a subset of the global model, the North and Equatorial Atlantic model domain extends meridionally from 28°S to the Fram Strait at 80°N. No inflow or outflow is prescribed at the northern and southern boundaries. Within a buffer zone of about 3° from the northern and southern boundaries, the 3-D model temperature, salinity, and depth of isopycnal interface are restored to the monthly GDEM with an *e*-folding time of 5–60 days that increases with distance from the boundary. Vertically, the Atlantic simulation has the conventional 32 layers whereas the global model has 41 layers (both in σ_2). The additional nine layers in the global configuration are all near the surface to better resolve the seasonal thermocline in the western Pacific Ocean. On one hand, the Atlantic simulation exhibits an improved vertical structure of the AMOC because of a finer vertical resolution in the deep Atlantic Ocean by using different reference densities near the bottom [*Xu et al*., 2012]. On the other hand, the global simulation shows improved water property (salinity in particular) in the upper layers of the Labrador Sea because it is coupled to the Community Ice CodE (CICE) of *Hunke and Lipscomb* [2008], instead of the simple energy loan sea ice parameterization [*Semtner*, 1976] used in the Atlantic simulation.

3. Observed and Modeled AMOC Transport at 26.5°N and 41°N

In this section, we examine the observed and modeled AMOC at 26.5°N and 41°N in both the global and Atlantic simulations. With few limitations on spatial coverage and/or temporal resolution, model results can

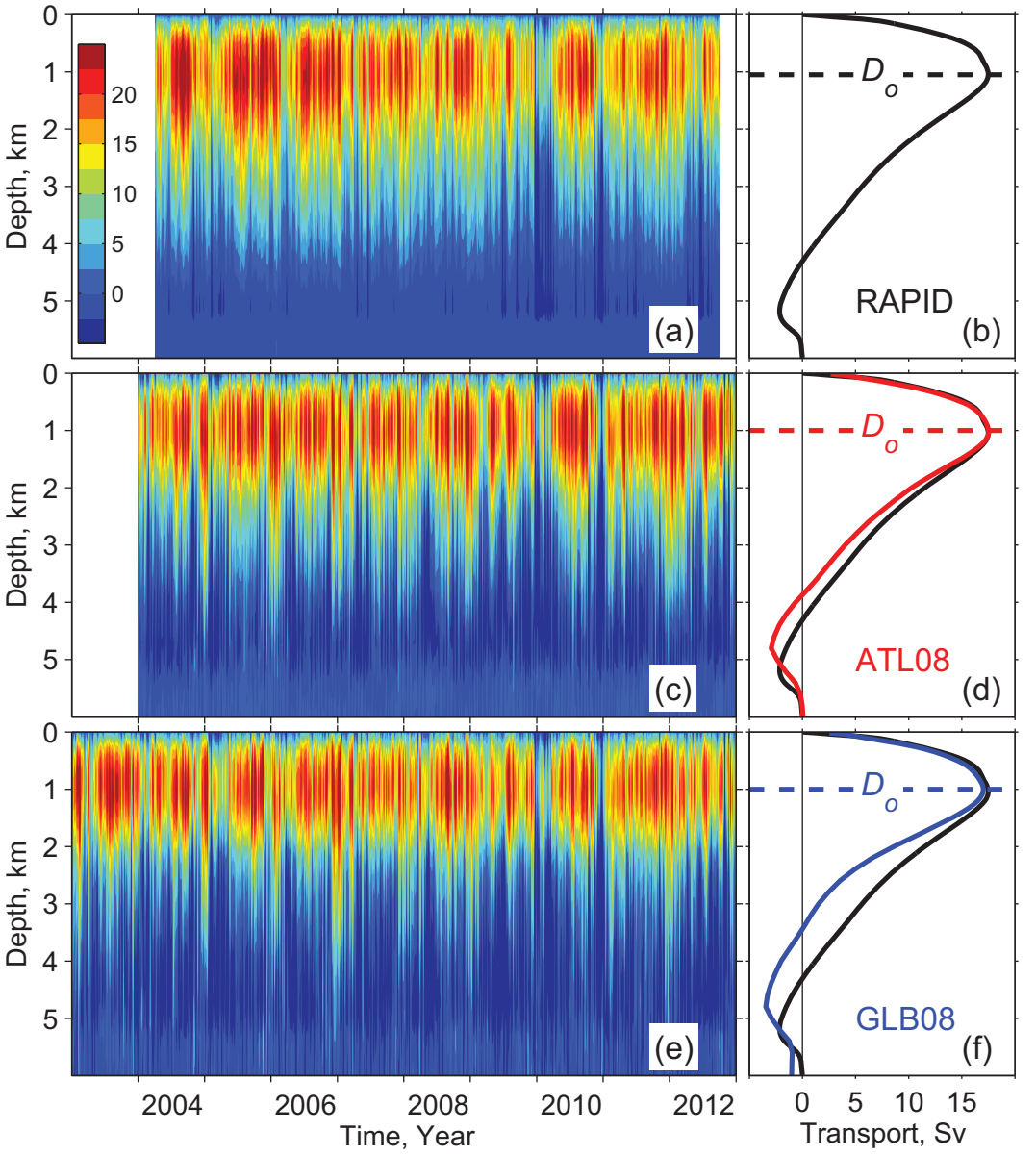

Figure 1. Streamfunction (Sv) of the Atlantic meridional overturning circulation at 26.5°N: (a, b) the RAPID observations; (c, d) the Atlantic HYCOM; and (e, f) the global HYCOM. Figures 1a, 1c, and 1e show the time series; Figures 1b, 1d, and 1f show the time-mean vertical profile from April 2004 to October 2012. The mean RAPID profile (black line) is overlaid on the HYCOM results. The overturning depth D_o, 1050 m in RAPID and 1000 m in both models, is determined as the depth of maximum overturning on the mean profile.

help place observations into a larger context of ocean circulation [e.g., *Xu et al.*, 2010, 2012, 2013]. In order to do so, however, it is critical that the model adequately represents the basic features of the observed AMOC, including its time-mean structure and temporal variability. Using the 1/12° North and Equatorial Atlantic configuration, *Xu et al.* [2012] showed that the time-mean structure of the AMOC and associated western boundary currents were consistent with the observations at 26.5°N. The temporal variability was however not discussed in *Xu et al.* [2012], nor was the AMOC transport at 41°N.

3.1. 26.5°N

Figures 1c–1e, f show the modeled time evolution and time average of the vertical structure of the overturning streamfunction across 26.5°N, in comparison to the RAPID observations (Figures 1a and 1b). From April 2004 to October 2012, the model and the observations exhibit a similar maximum overturning depth (D_O): 1050 m in the RAPID observations and 1000 m in both numerical simulations. The time mean AMOC

transport, defined as the streamfunction at D_O, is also similar: 17.5 Sv in the RAPID observations and the Atlantic simulation, and 17.0 Sv in the global simulation. Note that only the global simulation accounts for a $\sim$ 1 Sv southward net transport (Figure 1f) representing the flow from the Pacific to the Atlantic through the Bering Strait. In both simulations, the vertical transport structure of the northward limb (in the upper 1 km) is very close to the observations, whereas the southward limb is shallower by $\sim$ 400 m in the Atlantic model and $\sim$ 600 m in the global model. The discrepancy is most likely related to the model representation of both the southward Denmark Strait overflow water and the northward Antarctic bottom water.

Time series of the observed and modeled daily mean AMOC transports are compared in Figure 2. The model transports are low-passed with a fourth order, 10 day Butterworth filter as for the observations. Over the observational period (April 2004 to October 2012), both modeled AMOC transports have a standard deviation of 5.0 Sv, compared to 4.6 Sv in the RAPID observations. The modeled AMOC transport is well correlated with the RAPID observations, with a correlation coefficient R of $\sim$ 0.70 between the Atlantic/global model and the RAPID results (significant at 99.95% level). The correlation between the two modeled time series is high (R=0.84), implying that most of the model AMOC variability at 26.5°N is not influenced by dynamics outside of the Atlantic model domain.

3.1.1. AMOC Components

The observed AMOC transport is calculated as the sum of the Florida Current, the Ekman, and the mid-ocean transports (see section 2). The model's ability to represent these individual components is examined in Figures 3 and 4. The Florida Current in both the Atlantic and global simulations has a mean transport that is $\sim$ 2 Sv lower than in observations, but it has a similar standard deviation (Figures 3a and 4a). Both modeled Florida Current transports are in good agreement with the observations (R=0.49 and 0.42, respectively, significant at 99.95% level).

The modeled Ekman velocity cannot be isolated from the wind and thermohaline-driven velocity. The model Ekman transport is therefore estimated from the zonal wind stress that was used to force the simulations, as for the RAPID measurements. In essence, we are comparing the wind stresses used in RAPID and in the model simulations. The comparison in Figures 3b shows that the two wind stresses (see section 2 for details) are very similar at 26.5°N (R = 0.95, with slightly lower mean and higher standard deviation values for the modeled Ekman transport).

The modeled mid-ocean transport is calculated by integrating the meridional velocity fields across the basin from Abaco to the western Africa coast and removing the Ekman transport estimated from the wind stress. In the RAPID observations, it is estimated as the combination of a) directly measured transports of the western boundary current over the Bahamas escarpment [*Johns et al*., 2008], and b) geostrophic transports across the rest of the basin based on moored dynamic height data. Figures 3c and 4c show that the correlation of mid-ocean transport between the Atlantic/global model and the RAPID observations is of the same order as of the Florida Current (R=0.39 and 0.47, respectively, significant at 99% level).

The combination of the Florida Current and the mid-ocean transports, sometimes also termed as the AMOC minus Ekman transport, is the AMOC transport contribution that is derived from oceanic observations (Ekman transport is from atmospheric wind field observations) and accounts for most of the mean AMOC transport at 26.5°N. The correlation between the model results and the observations is of the same order as of the individual components (R=0.45 and 0.48, respectively, significant at 99.5% level; see Figures 3d and 4d).

Overall, both the Atlantic and global models simulate well the observed AMOC variability at 26.5°N. Variability of the individual components used to derive the observed AMOC transports is also well represented in both simulations. The global model shows a slightly better agreement with the observed mid-ocean and AMOC minus Ekman transports. This is probably due to a finer vertical resolution near the surface in the global configuration, leading to an improved Ekman transport (closer to that estimated from the wind stress). The reason for a slightly better representation of the Florida Current variability in the Atlantic model is unclear.

3.1.2. Time Scale Decomposition

The transports discussed in Figures 2–4 contain variability over a wide range of time scales. In order to investigate if these variabilities are similarly represented in the models, we decompose the transport signals

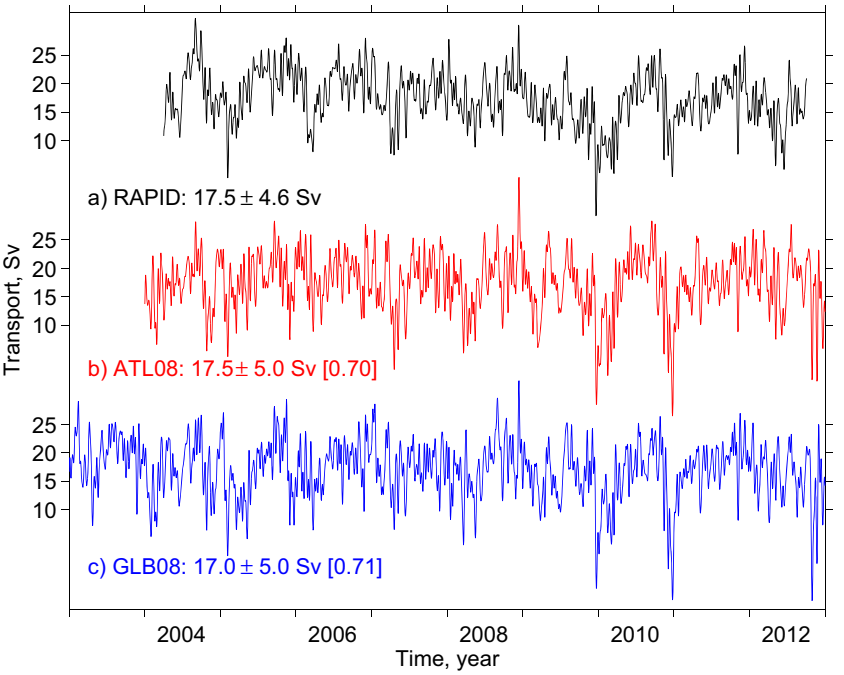

Figure 2. Time series of the AMOC transport at 26.5°N, defined as the streamfunction at maximum overturning depth D_o (Figure 1): (a) the RAPID observations (black), (b) Atlantic HYCOM (red), and (c) global HYCOM (blue). The colored numbers are the mean ± standard deviation values for transports from April 2004 to October 2012. The bracketed numbers are correlation coefficient (R) between the model and the RAPID time series. The R between two models is 0.84.

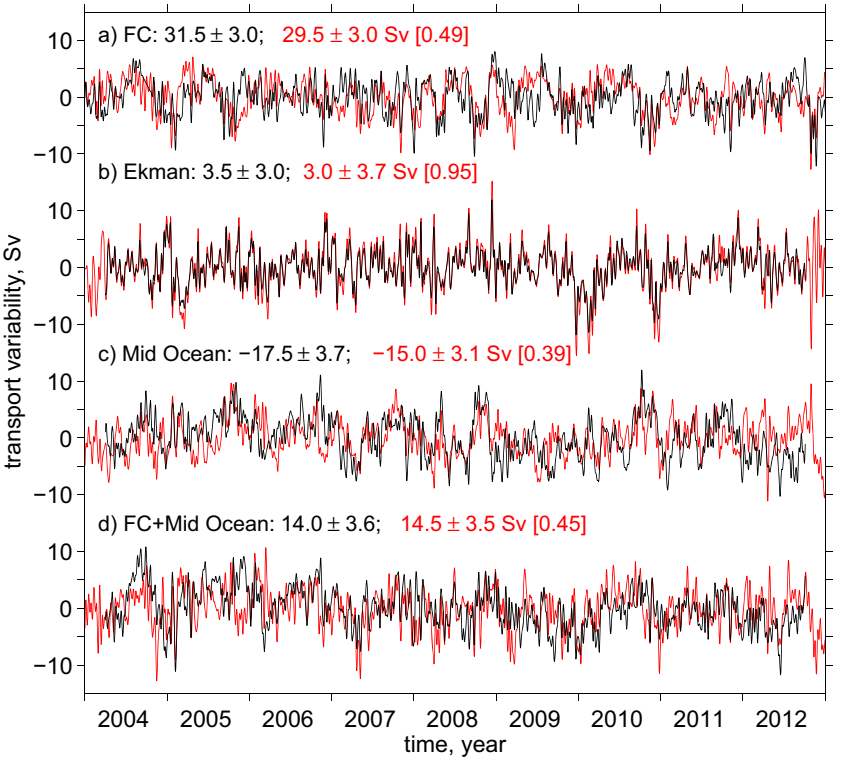

Figure 3. Transport variations of the AMOC components at 26.5°N: (a) the Florida Current (FC), (b) the Ekman transport, (c) the mid-ocean transport from Abaco Island, Bahamas to Africa, and (d) the combination of FC and mid-ocean transports (sometimes termed the AMOC minus Ekman transport). Black and red lines are results based on the RAPID observations and the Atlantic simulation, respectively. The colored numbers denote the mean ± standard deviation values. The bracketed numbers are the correlation coefficient between observations and model time series.

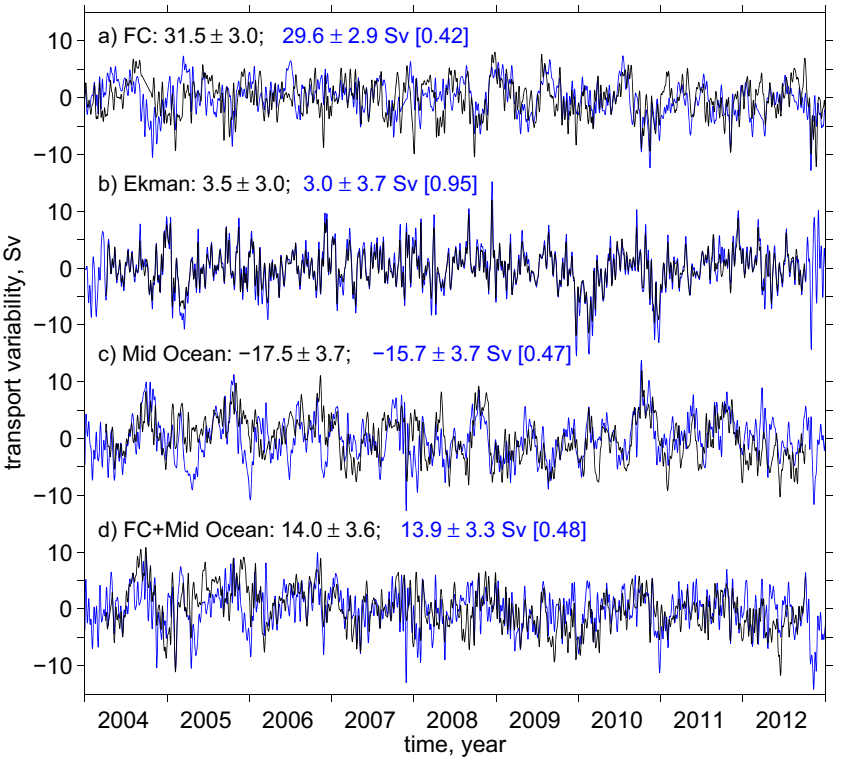

Figure 4. The same as in Figure 3 except that the model results (blue) are based on the global simulations.

with the ensemble empirical mode decomposition (EEMD) developed by *Huang and Wu* [2008] and *Wu and Huang* [2009]. The EEMD extracts the amplitude-frequency modulated oscillatory components (termed the intrinsic mode functions, or IMFs), successively from the highest to the lowest frequencies, without using a priori determined basis function. The number of IMFs is the integer of the binary logarithm of the time series length N ($\log_2$ N). The frequency and amplitude of each IMF are determined adaptively from the local characteristics of the time series and vary as a function of time. This is the advantage of EEMD over other methods in analyzing nonlinear and nonstationary signals.

The IMFs of the observed and the modeled AMOC and Florida Current transports are displayed in Figure 5. The typical period ranges from about 10 to 20 days for the second and third IMFs (note that the first IMF is close to zero because the signals have been low-pass filtered), from about 1 month to 6 months for the fourth to sixth IMFs, and from 1 year to several years for the 7th to 10th IMFs. The last (11th) IMF in Figure 5 represents the trend. The first 10 IMFs are combined in three components to further illustrate the variability on (a) high-frequency, (b) intraseasonal, and (c) seasonal and interannual time scales, respectively (see Figure 6 for detail).

Figures 5 and 6 show that the modeled AMOC transports in both the Atlantic and global simulations have a high variability on intraseasonal and shorter time scales, in good agreement with observations. The correlation coefficient R between the observed and modeled AMOC transports is about 0.7 for the high-frequency variability (Figure 6a) and 0.6 for the intraseasonal variability (Figure 6b), both significant at 99.95% level. The high-frequency variability in the Florida Current is well represented in both models (R of about 0.6, significant at 99.95% level). The intraseasonal variability is represented slightly better in the Atlantic (R of 0.50, significant at 99.95% level) than in the global (R of 0.36, significant at 99.5% level) simulation. Given that one usually associates the high-frequency and intraseasonal variability to random mesoscale events and eddies [*Frajka-Williams et al.*, 2013], it is somewhat surprising that the numerical models are able to simulate these short term variability of the AMOC and the Florida Current transports without data assimilation. The results suggest that these variabilities are primarily surface forced and that the wind may play a significant role.

The observed AMOC transports also exhibit a high variability on seasonal and some variability on interannual time scales, including a double dip of transport in the 2009/2010 [*McCarthy et al.*, 2012] and 2010/2011

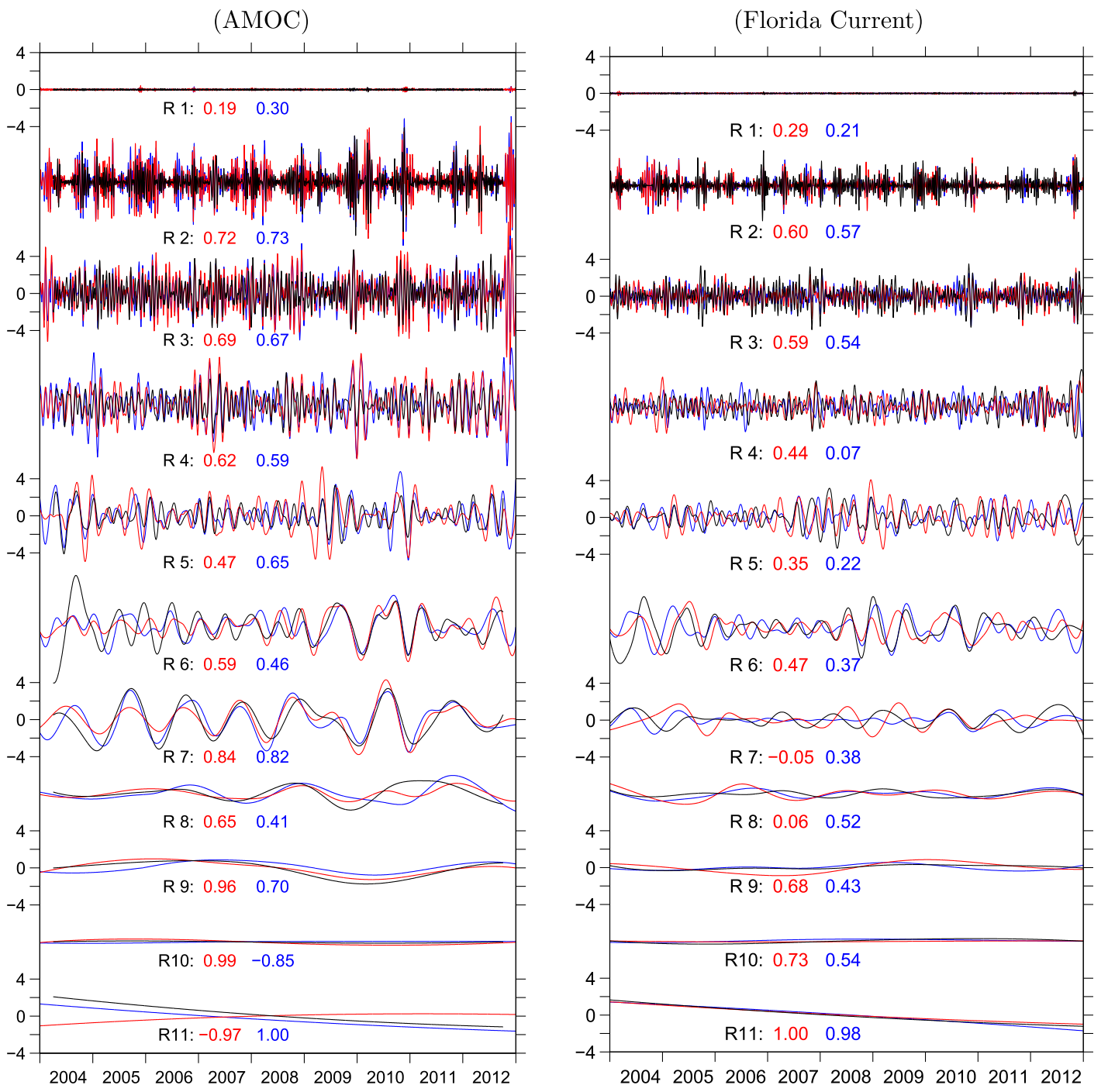

Figure 5. Transports of the AMOC and the Florida Current decomposed into 11 intrinsic mode functions (IMFs) of different time scales using the EEMD method by *Huang and Wu* [2008] and *Wu and Huang*, [2009]. The black, red, and blue lines are results from the RAPID observations, the Atlantic HYCOM, and the global HYCOM, respectively. For each IMF the colored numbers are the correlation coefficient R between the model and the RAPID time series.

winters. This seasonal and interannual variability is also well represented in the Atlantic and global simulations (R=0.86 and 0.75, respectively, significant at 99.95% level). For the Florida Current, the seasonal and interannual variability is relatively low in both the observations and models. A better correlation between the observed and modeled time series is found in the global simulation (R=0.46, significant at 95% level) than in the Atlantic simulation (R=0.26, insignificant at 95% level).

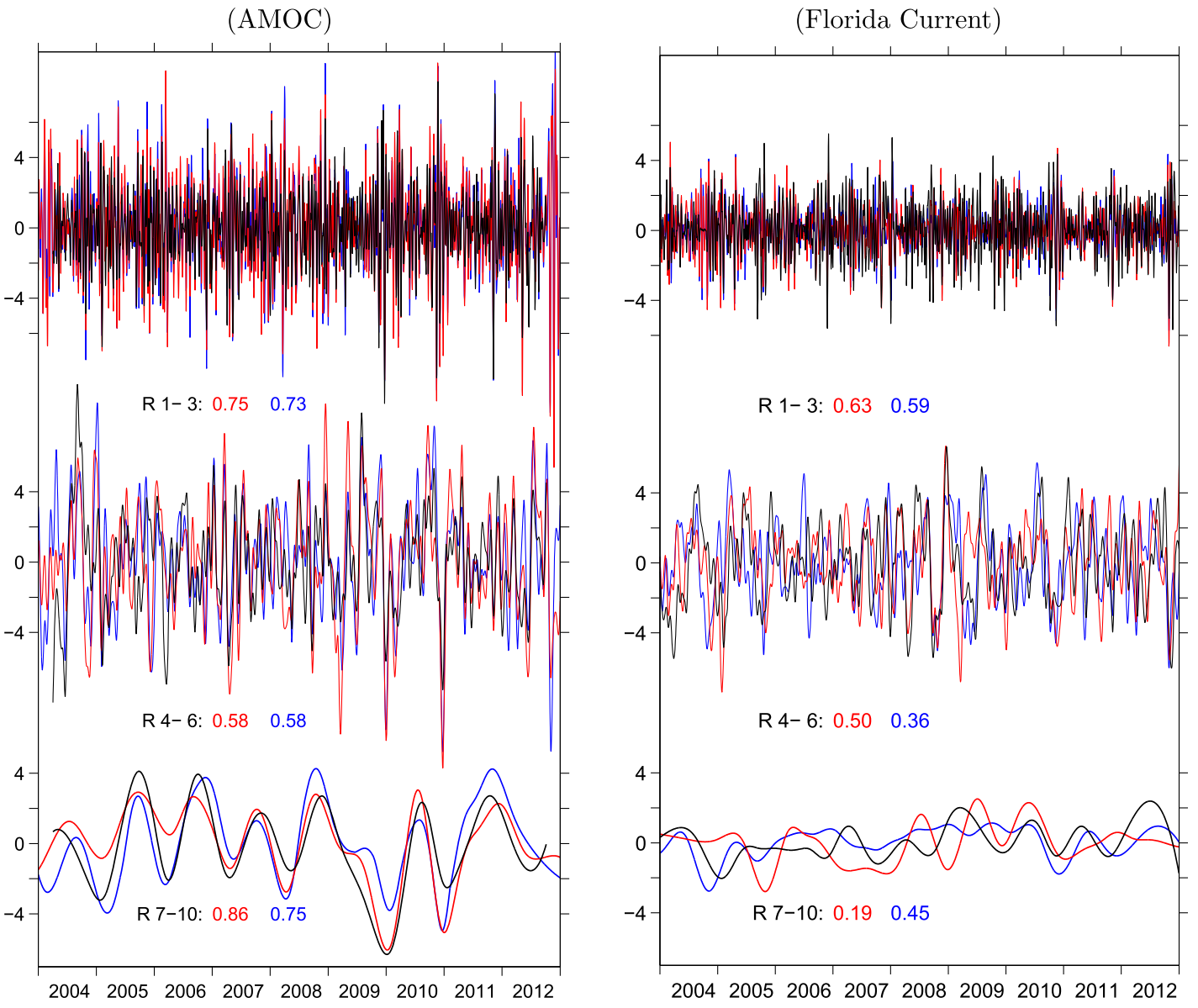

Figure 6. Similar to the Figure 5 but the intrinsic mode functions (IMFs) are summed to illustrate the variability on three general time scales: a) high frequency (IMFs 1–3, period of 3 weeks or shorter); (b) intraseasonal (IMFs 4–6, period of 1–6 months); and (c) seasonal and interannual (IMFs 7–10).

The last IMF in Figure 5 represents the long-term trend of the variability. For the RAPID period from April 2004 to October 2012, the observed AMOC and the Florida Current transports decreased 3.2 and 3.1 Sv, respectively. These long-term decreases are represented in the global simulation, with a decrease of 2.8 Sv for the AMOC and 3.1 Sv for the Florida Current. They are not as well represented in the Atlantic model since the AMOC transport increases slightly (0.9 Sv) while the Florida Current transport decreases (2.1 Sv) between 2004 and 2012. A more consistent result in the global simulation implies that the long-term variability may be influenced by dynamics outside the Atlantic model domain.

Although a decrease of about 3 Sv in the AMOC transport over eight and a half years is significant for a mean value of about 17 Sv, it is important to note that the length of time series is too short to determine if the decrease is part of a decadal/interdecadal variability or a long-term trend. The Florida Current transport also decreased about 3 Sv over the RAPID observation period, but applying the same decomposition method to its full time series yields a decreasing "trend" of 1 Sv from 1982 to 2012, which is really small when compared to the mean transport of about 32 Sv and is within the measurement uncertainty.

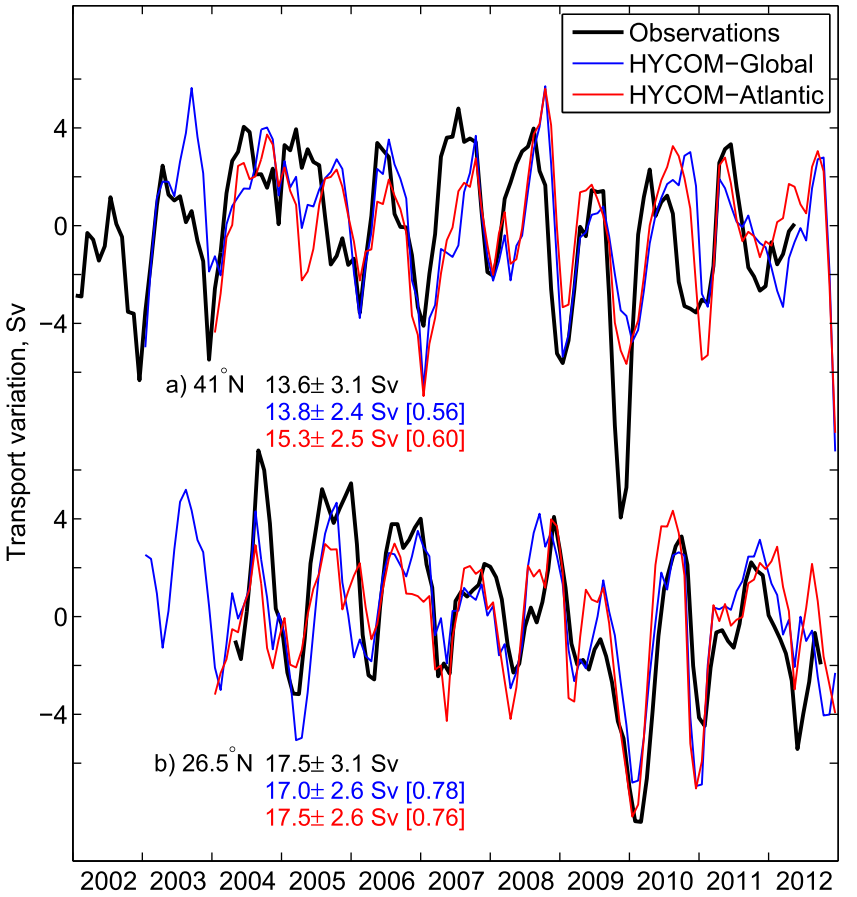

Figure 7. Variations of the monthly mean AMOC transport at (a) 41°N and (b) 26.5°N. The black, red, and blue lines are results based on the observations, the Atlantic model, and the global model, respectively. The colored numbers are the mean ± standard deviation values for the transports from April 2004 to April 2012. The bracketed numbers are correlation coefficient R between the modeled and observed time series. The R between two models is 0.83 at 26°N and 0.86 at 41°N.

3.2. 41°N

The observed and modeled monthly mean AMOC transports at 41°N are shown in Figure 7a. A 3 month running average is applied for the model time series to match the observational results [*Willis*, 2010]. The magnitude of the global model mean transport at 41°N is close to the observations, whereas the Atlantic model has a higher mean transport. The standard deviation of the transports is about 2.5 Sv in both simulations, compared to 3.1 Sv in observations. Both modeled time series correlate with the observations at zero lag (R=0.60 and 0.56, respectively, significant at 99.5% level). The highest correlation between models and observations is found when the model time series are lagged by 1 month (R=0.65 for both models, significant at 99.95% level). The two model time series are highly correlated with each other (R=0.86 with no time lag, significant at 99.95% level).

As for the observations, we can separate the modeled AMOC transport into contributions due to Ekman and geostrophy. As at 26.5°N, the wind stresses used in observations and in the models to compute the Ekman transport at 41°N are very similar and correlate highly with each other (R=0.99 for the monthly mean time series in Figure 8a). Contrary to 26.5°N, we do not find any correlation between the observed and modeled non-Ekman transport time series (Figure 8b). The Ekman transport variability at 41°N is of the same magnitude as of the geostrophic transport variability and is responsible for the ∼ 0.6 correlation between the observed and modeled AMOC variability (Figure 7a). Some correlation (at 95% level) is found between the modeled and observed geostrophic transports at 41°N when the model time series are shifted by about 6 months. *Mielke et al*. [2013] found a similar 6 month phase shift in the seasonal variation of the geostrophic transports between the observations and the global simulation of *von Storch et al*. [2012]. This lack of agreement between models and observations suggests that either the models do not adequately

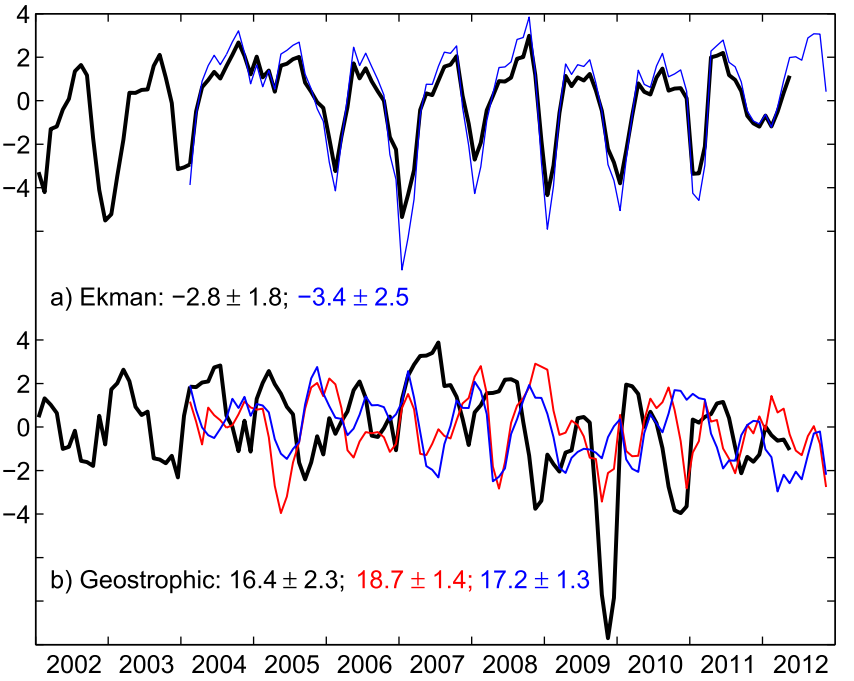

Figure 8. Variations of (a) Ekman and (b) Geostrophic (AMOC-Ekman) transports at 41°N. The black, red, and blue lines are results based on the observations, the Atlantic model, and the global model, respectively. The colored numbers are the mean ± standard deviation values. The Ekman transport is identical for two models.

represent the ocean dynamics at 41°N and/or the Argo floats are not able to sample adequately the AMOC variability.

In Figure 9a, the observed and modeled AMOC transport time series at 41°N are decomposed into 6 IMF components of different time scales using the same EEMD method used for 26.5°N. The first IMF exhibit some intraseasonal variability, but it is not well resolved since a 3 month running average was applied to the time series. The second IMF is the seasonal variability, which is dominant in both the observed and modeled time series. The highest correlation between the modeled and observed seasonal variability is found with a time lag of 1 month in the Atlantic model (0.84) and 2 months in the global model (0.71). The interannual variability (third to fifth IMFs) at 41°N is generally weaker than the seasonal variability. The third IMF is better represented in the global simulation than in the Atlantic simulation; the fourth IMF is represented to some extent in both simulations; and the fifth IMF is not represented in either simulations. In contrast to 26.5°N, neither the observations nor the model results at 41°N exhibits a trend from 2004 to 2012 (sixth IMF in Figure 9a).

3.3. Comparison of the AMOC Time Series at 26.5°N and 41°N

In this subsection, we compare the observed and modeled 3 month running averaged AMOC transport time series at 26.5°N and 41°N (Figures 7 and 9). Both the observations and models show a lower mean AMOC transport at 41°N than at 26.5°N. The standard deviation of the AMOC transports is similar between two latitudes, even though the values are lower in models than in observations.

Table 1. Correlation Coefficient of the AMOC Transports Between 41°N and 26.5°N in Observations as Well as in Numerical Simulations[a]

AMOC Transport	Total	Second IMF	Third IMF	Fourth IMF
Observations	0.67 [3]	0.66 [3]	0.72 [3]	0.65 [4]
Atlantic model	0.52 [0]	0.60 [0]	0.29 [−2]	0.49 [4]
Global model	0.40 [0]	0.66 [0]	0.39 [0]	0.28 [10]

[a]The bracketed numbers the time lag in month (positive for 41°N leading).

The correlation between the observed AMOC transport time series at 26.5°N and 41°N is highest when the 41°N time series lead by 3 months (R=0.67, significant at 99.95% level, Table 1). Separating the AMOC transport into Ekman and non-Ekman contributions, however, gives a lower correlation for each

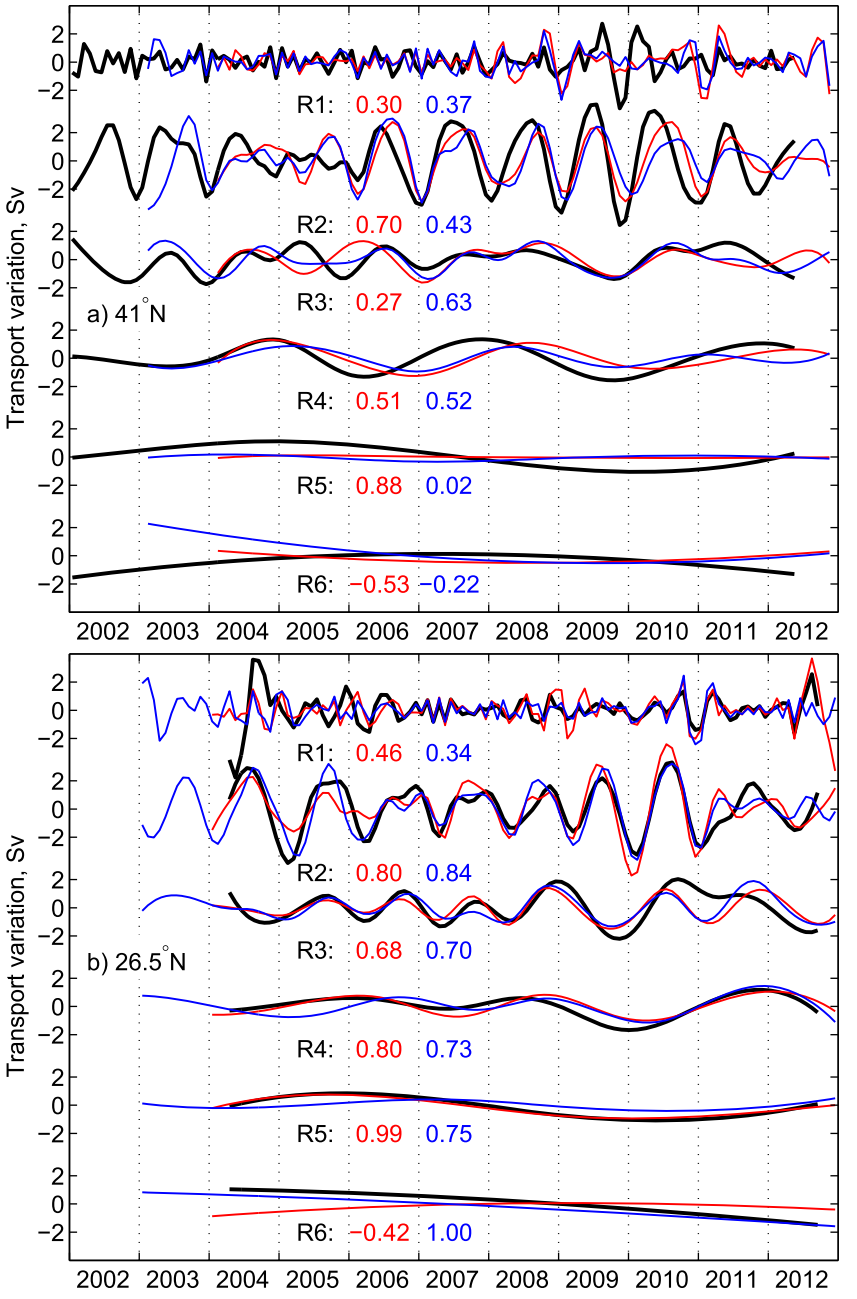

Figure 9. The monthly mean AMOC transports at (a) 41°N and (b) 26.5°N decomposed into 6 intrinsic mode functions (IMFs) using the EEMD method. The black, red, and blue lines are results from the observations, the Atlantic model, and the global model, respectively. For each IMF, the colored numbers are the zero-lagged correlation coefficient between the modeled and observed time series.

contribution. The highest correlation between the Ekman transport time series at these two latitudes is 0.34 (with 41°N leading by 2 months), whereas the highest correlation between the two non-Ekman transport time series is 0.46 (with 41°N leading by 4 months). This means that neither the Ekman nor non-Ekman component dominates the correlation between the variability at these two latitudes. The correlation between the modeled AMOC transport time series at two latitudes is lower than observed, with the highest correlation (R=0.52 and 0.40, respectively, significant at 97.5%) with no time lag.

In both the observations and the models, the variability is primarily on a seasonal time scale (second IMF in Figure 9), which is correlated in both observation and models (Table 1). On interannual time scales, the observations also exhibit a good correlation between these two latitudes (significant at 95% level) whereas the model results generally show insignificant correlation at 95% level.

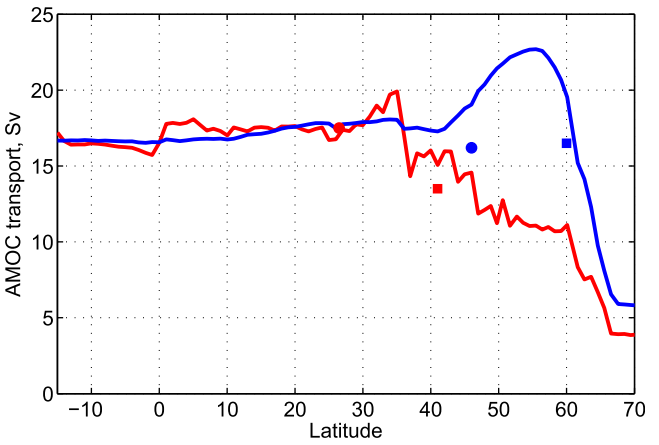

Figure 10. Time mean AMOC transport based on (red) depth and (blue) density coordinate as a function of latitude. Red circle and square are results based on RAPID and Argo data at 26.5°N and 41°N; blue circles and square are results based on repeat hydrographic data near 48°N [*Lumpkin et al.*, 2008] and 60°N [*Sarafanov et al.*, 2012].

4. Modeled Meridional Coherence of the AMOC Variability

Here we explore the meridional coherence of the AMOC transport beyond the 26.5°N and 41°N latitudes.

4.1. AMOC on Depth and Density Coordinates

The AMOC transports at 26.5°N and 41°N discussed until now were computed using depth coordinate, which we refer to as $AMOC_z$. The AMOC is also often computed using density coordinates ($AMOC_\sigma$), especially in the subpolar North Atlantic [e.g., *Lumpkin et al.*, 2008; *Lherminier et al.*, 2010; *Sarafanov et al.*, 2012]. The $AMOC_\sigma$ is representative of water mass transformation across isopycnals whereas the $AMOC_z$ is representative of vertical motion across fixed depths. The two definitions are pretty much equivalent as long as the isopycnals are relatively flat across the basin near the maximum overturning depth, which is the case in the tropical and subtropical regions (Figure 10). They however differ in the subpolar region where isopycnals slant upward across the basin from west to east. The $AMOC_z$ is smaller since a significant part of the northward transport in the east cancels the southward transport of the same depth in the west. This is not case for $AMOC_\sigma$ since these transports in the east and west have a large contrast in temperature/salinity (density) characteristics. *Zhang* [2010] showed that the meridional coherence of $AMOC_z$ and $AMOC_\sigma$ differs significantly on decadal time scales.

4.2. Meridional Coherence of the AMOC Transports on Various Time Scales

To examine the meridional coherence on different time scales, we calculate the modeled daily mean AMOC transports both in z and σ at every degree between 15°S and 70°N. The time series at each latitude is then decomposed into 11 IMF components with the EEMD. As shown in Figures 11–13, the patterns of the $AMOC_z$ and $AMOC_\sigma$ variability are overall quite similar, with the largest difference north of 40°N.

4.2.1. Intraseasonal Variability (Sixth IMF)

One cannot identify an overall consistent coherent pattern for intraseasonal variability (Figure 11), but on several instances, the variability is coherent over a large latitudinal range (up to 40°).

4.2.2. Seasonal Variability (Seventh IMF)

The seasonal variability shows two distinct coherent regimes (Figure 12): One north of 20°N, where the subpolar North Atlantic variability has the tendency to lead that of the subtropics; the other one is south of 20°N, with a much higher variability and opposite phase.

4.2.3. Interannual Variability (Ninth IMF)

An overall consistent coherent pattern cannot be identified for the interannual variability (Figure 13). However, as for the intraseasonal variability, the variability is often coherent over a large latitudinal range. The variability is weaker when compared to the variability on shorter time scales (Figures 11 and 12).

Since the AMOC is often separated into Ekman and geostrophic transports, it is interesting to examine the meridional coherence pattern of the individual components. Figures 12 and 14 show the seasonal variability of the $AMOC_z$ transport with and without the Ekman contribution, respectively. In the absence of the Ekman transport, the variability is significantly lower and the distinction between regimes north and south of 20°N disappears. This implies that the wind pattern are responsible for the lack of the coherence between the tropical and subtropical regions.

4.3. Vertical Structure of the High Variability in the Tropical Atlantic

One of the most striking feature in Figure 12 is the high seasonal variability of the AMOC transport south of 20°N in the tropical Atlantic. There is little knowledge about the AMOC variability in this region from

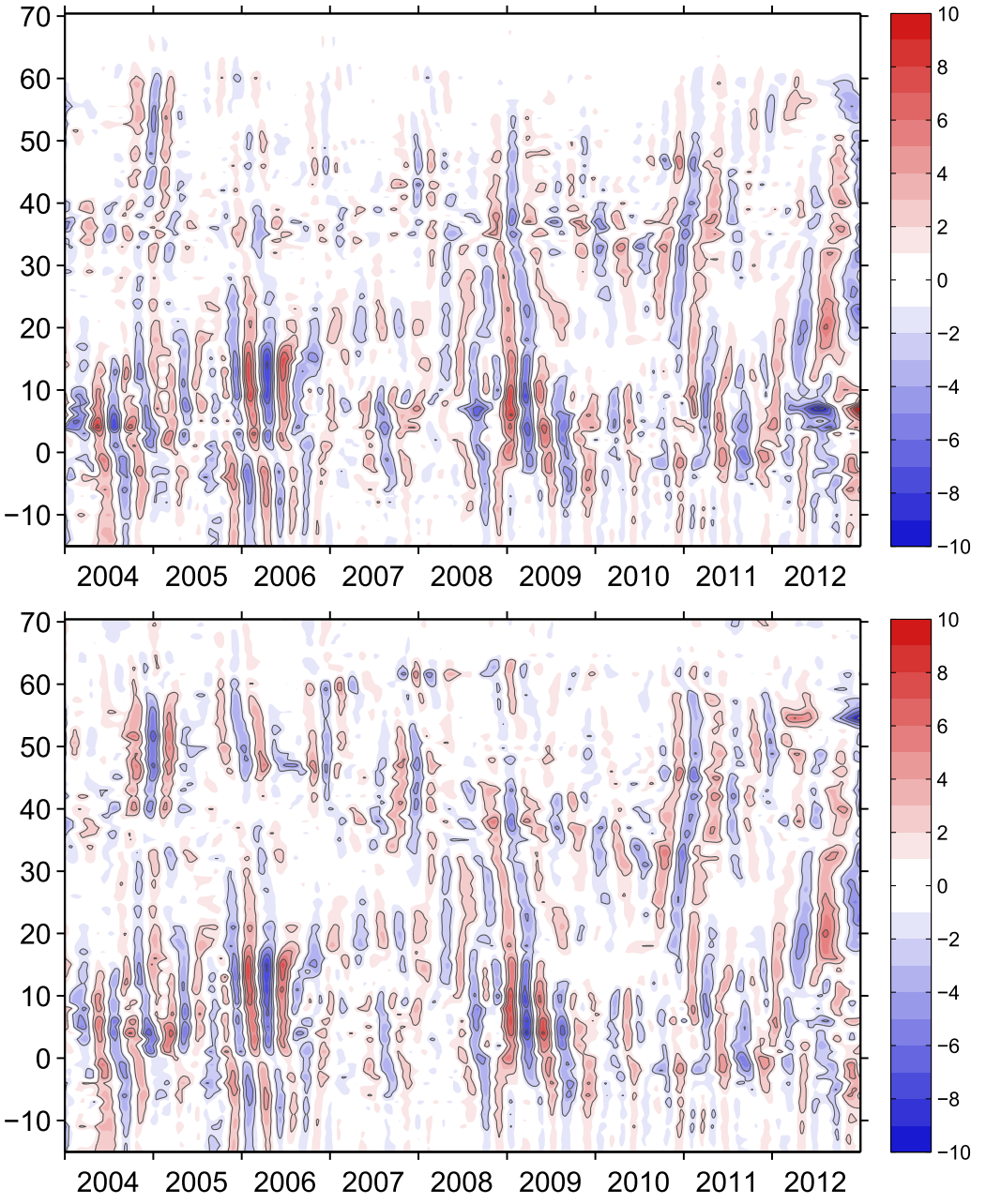

Figure 11. Intraseasonal variability of the AMOC transports as a function of latitude and time, based on the sixth IMF of the decomposed AMOC transport time series at each latitude. (top) AMOC$_z$ and (bottom) AMOCσ. Results from the Atlantic simulation (2004–2012).

observations. Figure 15 shows the 2004–2012 monthly mean volume transports across 10°N as a function of density. The AMOC consists of four water masses:

1. The near-surface water ($\sigma_2 \leq 32.60$) contributes a mean northward transport of 9.7 Sv with large variability: high in winter (17.5 Sv) and low in summer (−2 Sv). The transport fluctuations are driven by the Ekman transport variability (circles in Figure 14b).
2. The thermocline water ($32.60 < \sigma_2 \leq 35.15$) contributes a small mean northward transport of 1.6 Sv with small transport variability.
3. The Antarctic intermediate water (AAIW, $36.15 < \sigma_2 \leq 36.52$) contributes a mean northward transport of 5.5 Sv with a large variability: high in summer (9.6 Sv) and low in spring (1.7 Sv).
4. The North Atlantic Deep Water (NADW, $\sigma_2 > 36.52$) forms the core of the southward component of the AMOC.

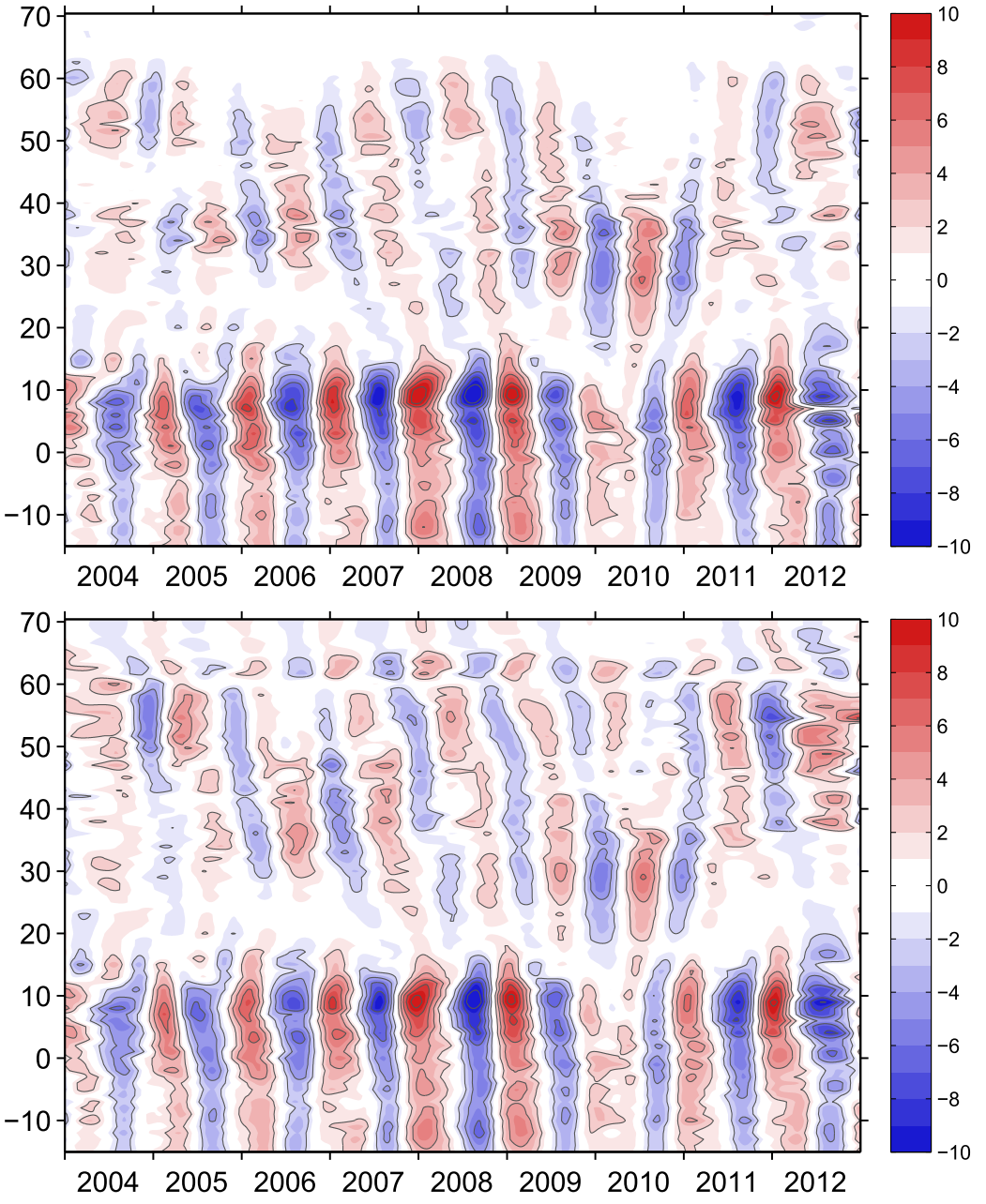

Figure 12. Seasonal variability of the AMOC transports as a function of latitude and time, based on the seventh IMF of the decomposed AMOC transport time series at each latitude. Results on (top) z and (bottom) σ, respectively. Results from the Atlantic simulation (2004–2012).

The high AMOC transport variability south of 20°N comes primarily from the Ekman transport variability of the near-surface water, and is modulated to some extent by the variability of the AAIW. The near-surface water transport also accounts for most of the heat transport mean and variability at 10°N. In addition to the high Ekman transport variability, the equatorial region also features fast propagating Rossby waves, which have a strong signature in the modeled AMOC and contribute to its high the high intraseasonal variability.

5. Summary and Discussion

Because of its large heat and freshwater transports and interaction with the atmosphere, the AMOC plays a fundamental role in establishing the mean state and the variability of Earth's climate. It is therefore important to understand the driving mechanisms behind the variability of the AMOC transport. In this study, we

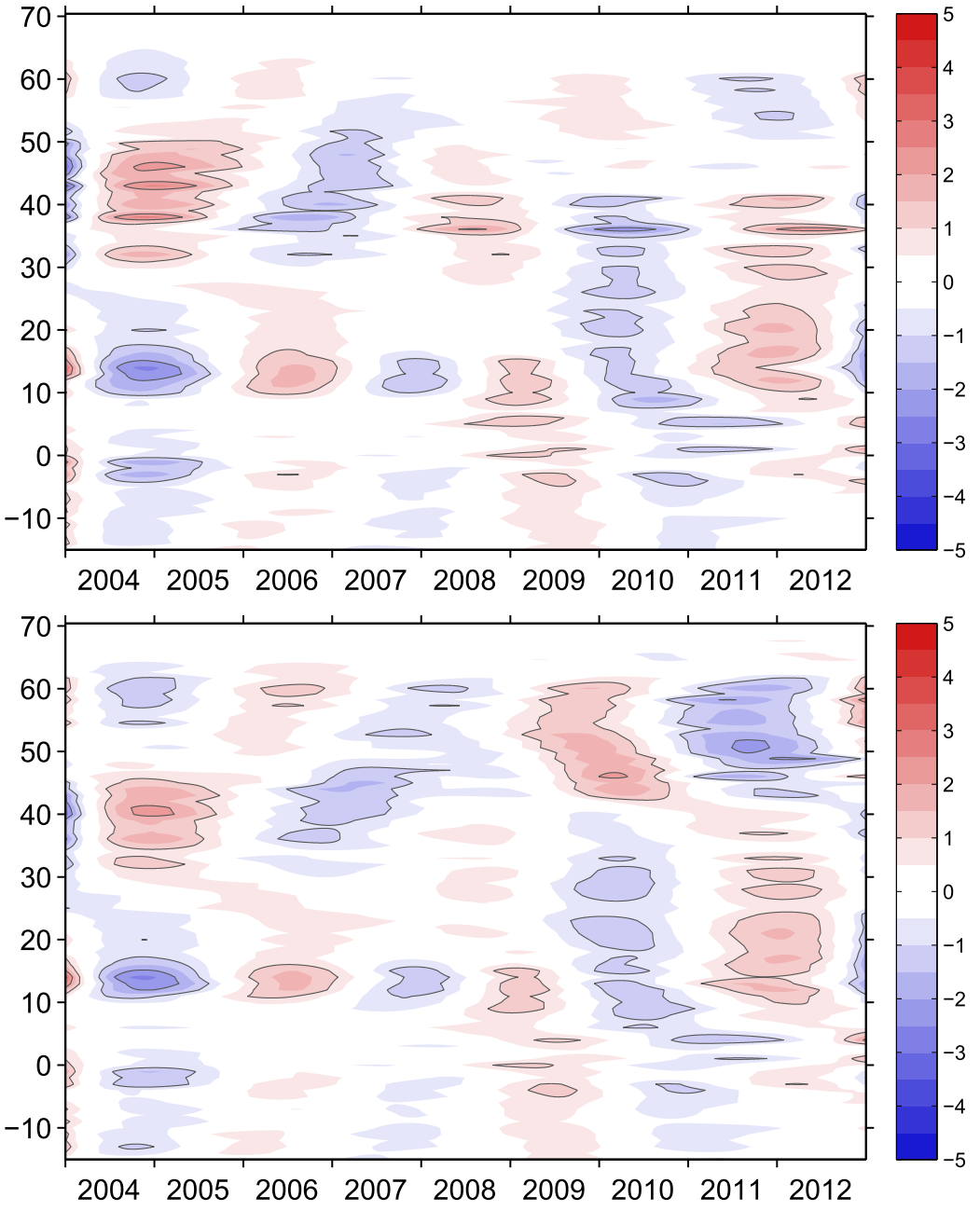

Figure 13. Interannual variability of the AMOC transports as a function of latitude and time, based on the ninth IMF of the decomposed AMOC transport time series at each latitude. Results on (top) z and (bottom) σ, respectively. Results from the Atlantic simulation (2004–2012).

used two 1/12° eddy-resolving HYCOM simulations together with observations at 26.5°N and 41°N to investigate the AMOC variability from intraseasonal to interannual time scales.

The model results are in very good agreement with the RAPID observations at 26.5°N. This is true not only for the total AMOC transports, but also for its components (the Florida Current, the mid-ocean, and Ekman transports). Both the models (global and Atlantic) simulate well the observed AMOC variability on intraseasonal, seasonal, and interannual time scales, but only the global model simulates the observed long-term decrease in the AMOC and the Florida Current transports (∼ 3 Sv over 2004–2012), suggesting that long time scale variability may be influenced by the dynamics outside the Atlantic model domain.

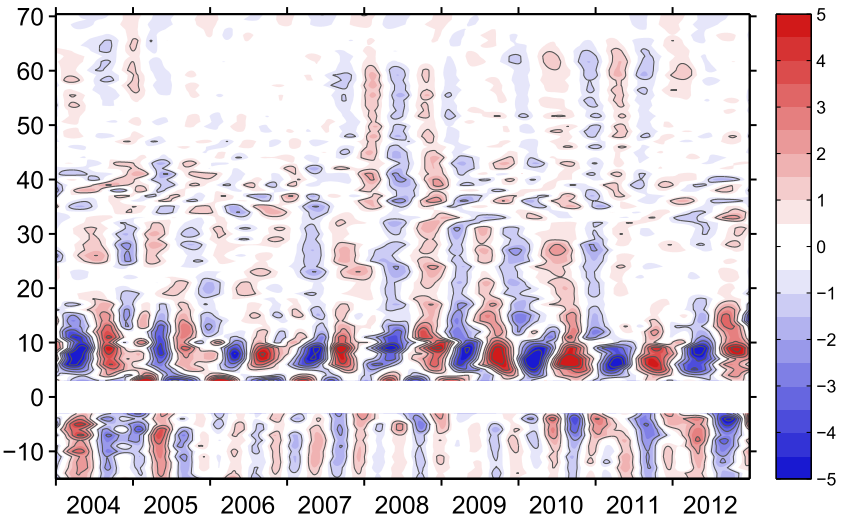

Figure 14. Similar as in Figure 12 for $AMOC_z$ but with the Ekman contribution (estimated from wind stress) removed.

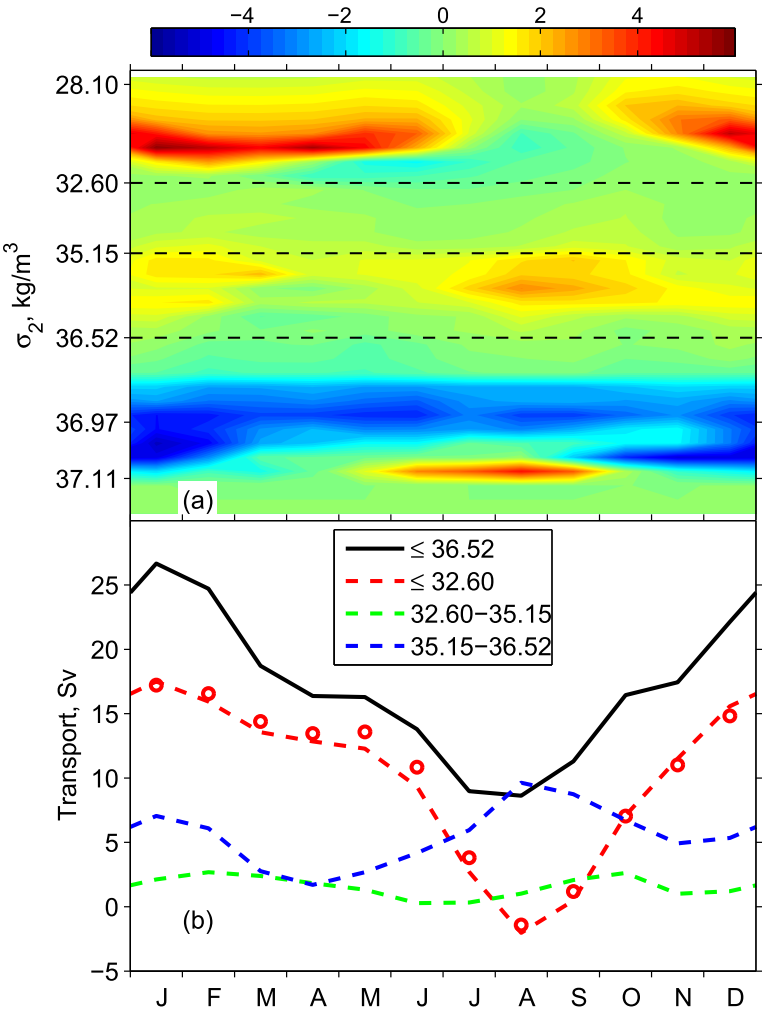

Figure 15. Monthly mean volume transports in Sv across 10°N from the 1/12° Atlantic simulation in 2004–2012. (a) The distribution as a function of time and density; (b) the transports of the three water masses (colored dash lines) in the top AMOC limb and their sum (black solid line). The transports of the bottom AMOC limb ($\sigma_2 > 36.52$) are the same as the black line but southward. Circles in Figure 15b denote the Ekman transport determined from model wind stress field.

At 41°N, however, the agreement between the model results and the observations is mostly due to the Ekman transports. The geostrophic transport is approximately 6 months out of phase. This result is similar to that of *Mielke et al*. [2013] who also found a 6 month phase shift in the seasonal variability of the geostrophic transport between the observations and the global simulation of *von Storch et al*. [2012]. Idealized two-layer model simulations show a similar discrepancy between the observed and modeled geostrophic transports (J. Zhao and J. Yang, personal communication, 2014). This lack of agreement between models and observations may suggest that the models do not adequately represent the ocean dynamics at 41°N, and consequently that the model-determined meridional coherence may be incorrect in high latitudes. It may also suggest that the Argo floats are not able to sample adequately the AMOC variability. It is a challenge latitude to accurately estimate the meridional transport since it is along the mean axis of the energetic Gulf Stream in which the eddy variability is among the highest of the world ocean.

The AMOC variability is overall very similar between the global and Atlantic simulations, which is not too surprising given that the same atmospheric forcing is used in both models. This also shows the dynamics outside the Atlantic model domain play a minimum role. Wind variability turns out to be the primary source for the AMOC variability, as suggested in *Roberts et al*. [2013] for interannual variability. The observed seasonal and interannual variability of the geostrophic transport at 26.5°N can be explained, using idealized two-layer model simulations, by the wind-driven subtropical gyre variability [*Zhao and Johns*, 2014a, 2014b]. In addition, the Ekman transport itself directly contributes to the AMOC variability: One example is the abnormally low AMOC transport in the 2009/2010 winter caused by the very low North Atlantic Oscillation [*Xu et al*., 2012; *Häkkinen and Rhines*, 2013].

The model results show that both observations and model results exhibit higher AMOC variability on seasonal and shorter time scales than on interannual and longer time scales. On intraseasonal and interannual time scales, the AMOC variability is often coherent over a wide latitudinal range, but no overall consistent coherent pattern between the Equator and 70°N can be identified on any of these time scales. The modeled interannual variability show similar pattern south of about 30°N (Figure 13), which is consistent with the recent study of *Kelly et al*. [2014], except that their coherence pattern extends further north, as in *Elipot et al*. [2014]. It should be noted that the time series (model and observation) are too short to draw definite conclusions on interannual and longer time scales variability. On seasonal time scales, the model AMOC variability exhibits two distinct coherent regimes north and south of 20°N. This is mostly contributed from the Ekman transport variability. In the tropical Atlantic, the high variability comes primarily from the near-surface water (Ekman), but is modulated to some extent by the transport of Antarctic Intermediate Water below the thermocline.

References

Acknowledgments
This work is supported by ONR award N00014-09-1-0587. Data from the RAPID/MOCHA monitoring project are funded by the Natural Environment Research Council (NERC) and National Science Foundation (NSF) and are available at http://www.rapid.ac.uk/rapidmoc. We thank Josh Willis and Will Hobbs for providing the 41°N results. The simulations are performed on supercomputers at the Navy DoD Supercomputing Resource Center (DSRC), Stennis Space Center, MS, using computer time provided by the U.S. DoD High Performance Computing Modernization Program. The model details and output are securely stored in the Navy DSRC archive server. Special thanks to Alan J. Wallcraft (NRL/SSC) for help in configuring the numerical experiments. This is NRL contribution NRL/JA/7320-14-2122, which is approved for public release and distribution is unlimited.

Atlas, R. M., R. N. Hoffman, J. Ardizzone, S. M. Leidner, J. C. Jusem, D. K. Smith, and D. Gombos (2011), A cross-calibrated, multi-platform ocean surface wind velocity product for meteorological and oceanographic applications, *Bull. Am. Meteorol. Soc.*, *92*, 157–174, doi:10.1175/2010BAMS2946.1.

Bingham, R. J., C. W. Hughes, V. Roussenov, and R. G. Williams (2007), Meridional coherence of the North Atlantic meridional overturning circulation, *Geophys. Res. Lett.*, *34*, L23606, doi:10.1029/2007GL031731.

Bleck, R. (2002), An oceanic general circulation model framed in hybrid isopycnic-Cartesian coordinates, *Ocean Modell.*, *37*, 55–88.

Böning, C. W., M. Scheinert, J. Dengg, A. Biastoch, and A. Funk (2006), Decadal variability of subpolar gyre transport and its reverberation in the North Atlantic overturning, *Geophys. Res. Lett.*, *33*, L21S01, doi:10.1029/2006GL026906.

Bryden, H. L., and M. M. Hall (1980), Heat transport by currents across 25°N latitude in the Atlantic Ocean, *Science*, *207*(4433), 884–886.

Bryden, H. L., and S. Imawaki (2001), Ocean heat transport, in *Ocean Circulation and Climate: Observing and Modelling the Global Ocean*, edited by G. Siedler, J. Church, and J. Gould, pp. 455–474, Academic, San Francisco, Calif.

Bryden, H. L., H. R. Longworth, and S. A. Cunningham (2005), Slowing of the Atlantic meridional overturning circulation at 25°N, *Nature*, *438*, 655–657, doi:10.1038/nature04385.

Carnes, M. R. (2009), Description and evaluation of GDEM-V3.0, *Tech. Rep. NRL/MR/7330–09–9165*, 21 pp., Naval Res. Lab, Stennis Space Center, Miss. [Available at http://www7320. nrlssc.navy.mil/pubs.php.]

Chassignet, E. P., L. T. Smith, G. R. Halliwell, and R. Bleck (2003), North Atlantic simulations with the hybrid coordinate ocean model (HYCOM): Impact of the vertical coordinate choice, reference pressure, and thermobaricity, *J. Phys. Oceanogr.*, *33*, 2504–2526.

Chassignet, E. P., et al. (2006), Generalized vertical coordinates for eddy-resolving global and coastal ocean forecasts, *Oceanography*, *19*(1), 20–31.

Cunningham, S. A., et al. (2007), Temporal variability of the Atlantic meridional overturning circulation at 26.5°N, *Science*, *317*, 935–938, doi:10.1126/science.1141304.

Dee, D. P., et al. (2011), The ERA-Interim reanalysis: Configuration and performance of the data assimilation system, *Q. J. R. Meteorol. Soc.*, *137*(656), 553–597, doi:10.1002/qj.828.

Delworth, T. L., R. Zhang, and M. E. Mann (2007), Decadal to centennial variability of the Atlantic from observations and models, in *Ocean Circulation: Mechanisms and Impacts-Past and Future Changes of Meridional Overturning*, edited by A. Schmittner, J. C. H. Chiang, and S. R. Hemming, pp. 131–148, AGU, Washington, D. C., doi:10.1029/173GM10.

Elipot, S., E. Frajka-Williams, C. W. Hughes, and J. K. Willis (2014), The observed North Atlantic meridional overturning circulation: Its meridional coherence and ocean bottom pressure, *J. Phys. Oceanogr.*, *44*, 517–537, doi:10.1175/JPO-D-13-026.1.
Frajka-Williams, E., W. E. Johns, C. S. Meinen, L. M. Beal, and S. A. Cunningham (2013), Eddy impacts on the Florida Current, *Geophys. Res. Lett.*, *40*, 349–353, doi:10.1002/grl.50115.
Ganachaud, A., and C. Wunsch (2000), Improved estimates of global ocean circulation, heat transport, and mixing from hydrographic data, *Nature*, *408*, 453–456.
Häkkinen, S., and P. B. Rhines (2013), Northern North Atlantic sea surface height and ocean heat content variability, *J. Geophys. Res. Oceans*, *118*, 3670–3678, doi:10.1002/jgrc.20268.
Hall, M. M., and H. L. Bryden (1982), Direct estimates and mechanisms of ocean heat transport, *Deep Sea Res., Part A*, *29*(3), 339–359.
Hobbs, W. R., and J. K. Willis (2012), Midlatitude North Atlantic heat transport: A time series based on satellite and drifter data, *J. Geophys. Res.*, *117*, C01008, doi:10.1029/2011JC007039.
Holland, D. M., R. H. Thomas, B. De Young, M. H. Ribergaard, and B. Lyberth (2008), Acceleration of Jakobshavn Isbræ triggered by warm subsurface ocean waters, *Nat. Geosci.*, *1*(10), 659–664, doi:10.1038/ngeo316.
Huang, N. E., and Z. Wu (2008), A review on Hilbert-Huang transform: Method and its applications to geophysical studies, *Rev. Geophys.*, *46*, RG2006, doi:10.1029/2007RG000228.
Hunke, E. C., and W. H. Lipscomb (2008), CICE: The Los Alamos sea ice model documentation and software user's manual, version 4.0, *Tech. Rep. LA-CC-06-012*, Los Alamos Natl. Lab., Los Alamos, N. M.
Johns, W. E., L. M. Beal, M. O. Baringer, J. R. Molina, S. A. Cunningham, T. Kanzow, and D. Rayner (2008), Variability of shallow and deep western boundary currents off the Bahamas during 2004-05: Results from the 26°N RAPID-MOC Array, *J. Phys. Oceanogr.*, *38*, 605–623, doi:10.1175/2007JPO3791.1.
Johns, W. E., et al. (2011), Continuous, array-based estimates of Atlantic Ocean heat transport at 26.5°N, *J. Clim.*, *24*(10), 2429–2449, doi:10.1175/2010JCLI3997.1.
Kanzow, T., U. Send, W. Zenk, A. D. Chave, and M. Rhein (2006), Monitoring the integrated deep meridional flow in the tropical North Atlantic: Long-term performance of a geostrophic array, *Deep Sea Res., Part I*, *53*(3), 528–546, doi:10.1016/j.dsr.2005.12.007.
Kanzow, T., et al. (2007), Observed flow compensation associated with the MOC at 26.5°N in the Atlantic, *Science*, *317*, 938–941.
Kanzow, T., U. Send, and M. McCartney (2008), On the variability of the deep meridional transports in the tropical North Atlantic, *Deep Sea Res., Part I*, *55*(12), 1601–1623, doi:10.1016/j.dsr.2008.07.011.
Kanzow, T., et al. (2010), Seasonal variability of the Atlantic meridional overturning circulation at 26.5°N, *J. Clim.*, *23*(21), 5678–5698, doi:10.1175/2010JCL13389.1.
Kelly, K. A., L. Thompson, and J. Lyman (2014), The coherence and impact of meridional heat transport anomalies in the Atlantic Ocean inferred from observations, *J. Clim.*, *27*, 1469–1487, doi:10.1175/JCLI-D-12-00131.1.
Knight, J. R., R. J. Allan, C. K. Folland, M. Vellinga, and M. E. Mann (2005), A signature of persistent natural thermohaline circulation cycles in observed climate, *Geophys. Res. Lett.*, *32*, L20708, doi:10.1029/2005GL024233.
Koltermann, K. P., A. V. Sokov, V. P. Tereschenkov, S. A. Dobroliubov, K. Lorbacher, and A. Sy (1999), Decadal changes in the thermohaline circulation of the North Atlantic, *Deep Sea Res., Part II*, *46*, 109–138.
Kuhlbrodt, T., A. Griesel, M. Montoya, A. Levermann, M. Hofmann, and S. Rahmstorf (2007), On the driving processes of the Atlantic meridional overturning circulation, *Rev. Geophys.*, *45*, RG2001, doi:10.1029/2004RG000166.
LeBel, D. A., et al. (2008), The formation rate of North Atlantic Deep Water and Eighteen Degree Water calculated from CFC-11 inventories observed during WOCE, *Deep Sea Res., Part I*, *55*(8), 891–910, doi:10.1016/j.dsr.2008.03.009.
Lherminier, P., H. Mercier, T. Huck, C. Gourcuff, F. F. Perez, P. Morin, A. Sarafanov, and A. Falina (2010), The Atlantic meridional overturning circulation and the subpolar gyre observed at the A25-OVIDE section in June 2002 and 2004, *Deep Sea Res., Part I*, *57*, 1374–1391, doi:10.1016/j.dsr.2010.07.009.
Longworth, H. R., and H. L. Bryden (2007), Discovery and quantification of the Atlantic meridional overturning circulation: The importance of 25°N, in *Ocean Circulation: Mechanisms and Impacts-Past and Future Changes of Meridional Overturning*, edited by A. Schmittner, J. C. H. Chiang, and S. R. Hemming, pp. 5–18, AGU, Washington, D. C., doi:10.1029/173GM03.
Lorbacher, K., and K. P. Koltermann (2000), Subinertial variability of transport estimates across 48°N in the Atantic Ocean, *Int. WOCE Newslett.*, *40*, 3–5.
Lozier, M. S. (2010), Deconstructing the conveyor belt, *Science*, *328*, 1507–1511, doi:10.1126/science.1189250.
Lozier, M. S. (2012), Overturning in the North Atlantic, *Annu. Rev. Mar. Sci.*, *4*, 291–315, doi:10.1146/annurev-marine-120710-100740.
Lumpkin, R., and K. G. Speer (2003), Large scale vertical and horizontal circulation in the North Atlantic Ocean, *J. Phys. Oceanogr.*, *33*, 1902–1920.
Lumpkin, R., K. G. Speer, and K. P. Koltermann (2008), Transport across 48°N in the Atlantic Ocean, *J. Phys. Oceanogr.*, *38*, 733–752, doi:10.1175/JPO3636.1.
McCarthy, G., et al. (2012), Observed interannual variability of the Atlantic meridional overturning circulation at 26.5°N, *Geophys. Res. Lett.*, *39*, L19609, doi:10.1029/2012GL052933.
Meinen, C. S., M. O. Baringer, and R. F. Garcia (2010), Florida Current transport variability: An analysis of annual and longer-period signals, *Deep Sea Res., Part I*, *57*, 835–846, doi:10.1016/j.dsr.2010.04.001.
Mielke, C., E. Frajka-Williams, and J. Baehr (2013), Observed and simulated variability of the AMOC at 26°N and 41°N, *Geophys. Res. Lett.*, *40*, 1159–1164, doi:10.1002/grl.50233.
Rayner, D., et al. (2011), Monitoring the Atlantic meridional overturning circulation, *Deep Sea Res., Part II*, *58*(17), 1744–1753, doi:10.1016/j.dsr2.2010.10.056.
Rhines, P. B., S. Häkkinen, and S. A. Josey (2008), Is oceanic heat transport significant in the climate system, in *Arctic-Subarctic Ocean Fluxes: Defining the Role of the Northern Seas in Climate*, edited by R. R. Dickson, J. Meincke, and P. B. Rhines, pp. 87–109, Springer, N. Y.
Richardson, P. L. (2008), On the history of meridional overturning circulation schematic diagrams, *Progr. Oceanogr.*, *76*(4), 466–486, doi:10.1016/j.pocean.2008.01.005.
Roberts, C. D., et al. (2013), Atmosphere drives recent interannual variability of the Atlantic meridional overturning circulation at 26.5°N, *Geophys. Res. Lett.*, *40*, 5164–5170, doi:10.1002/grl.50930.
Roemmich, D. (1980), Estimation of meridional heat flux in the North Atlantic by inverse methods, *J. Phys. Oceanogr.*, *10*, 1972–1983.
Roemmich, D., and C. Wunsch (1985), Two transatlantic sections: meridional circulation and heat flux in the subtropical North Atlantic Ocean, *Deep Sea Res., Part A*, *32*(6), 619–664.
Rosmond, T., J. Teixeira, M. Peng, T. Hogan, and R. Pauley (2002), Navy Operational Global Atmospheric Prediction System (NOGAPS): Forcing for ocean models, *Oceanography*, *15*(1), 99–108.

Sarafanov, A., A. Falina, H. Mercier, A. Sokov, P. Lherminier, C. Gourcuff, S. Gladyshev, F. Gaillard, and N. Daniault (2012), Mean full-depth summer circulation and transports at the northern periphery of the Atlantic Ocean in the 2000s, *J. Geophys. Res.*, *117*, C01014, doi: 10.1029/2011JC007572.

Semtner, A. J. (1976), A model for the thermodynamic growth of sea ice in numerical investigations of climate, *J. Phys. Oceanogr.*, *6*(3), 379–389.

Send, U., M. Lankhorst, and T. Kanzow (2011), Observation of decadal change in the Atlantic meridional overturning circulation using 10 years of continuous transport data, *Geophys. Res. Lett.*, *38*, L24606, doi:10.1029/2011GL049801.

Serreze, M. C., M. M. Holland, and J. Stroeve (2007), Perspectives on the Arctic's shrinking sea-ice cover, *Science*, *315*(5818), 1533–1536, doi: 10.1126/science.1139426.

Smeed, D. A., et al. (2014), Observed decline of the Atlantic meridional overturning circulation 2004–2012, *Ocean Sci.*, *10*(1), 29–38, doi: 10.5194/os-10-29-2014.

Smethie, W. M., and R. A. Fine (2001), Rates of North Atlantic Deep Water formation calculated from chlorofluorocarbon inventories, *Deep Sea Res., Part I*, *48*, 189–215.

Srokosz, M., M. Baringer, H. Bryden, S. Cunningham, T. Delworth, S. Lozier, J. Marotzke, and R. Sutton (2012), Past, present, and future changes in the Atlantic meridional overturning circulation, *Bull. Am. Meteorol. Soc.*, *93*(11), 1663–1676, doi:10.1175/BAMS-D-11-00151.1.

Straneo, F., G. S. Hamilton, D. A. Sutherland, L. A. Stearns, F. Davidson, M. O. Hammill, G. B. Stenson, and A. Rosing-Asvid (2010), Rapid circulation of warm subtropical waters in a major glacial fjord in East Greenland, *Nat. Geosci.*, *3*(3), 182–186, doi:10.1038/ngeo764.

Uppala, S. M., et al. (2005), The ERA-40 re-analysis, *Q. J. R. Meteorol. Soc.*, *131*, 2961–3012, doi:10.1256/qj.04.176.

von Storch, J.-S., C. Eden, I. Fast, H. Haak, D. Hernández-Deckers, E. Maier-Reimer, J. Marotzke, and D. Stammer (2012), An estimate of the Lorenz energy cycle for the world ocean based on the STORM/NCEP simulation, *J. Phys. Oceanogr.*, *42*(12), 2185–2205, doi:10.1175/JPO-D-12-079.1.

Willis, J. (2010), Can in situ floats and satellite altimeters detect long-term changes in Atlantic Ocean overturning, *Geophys. Res. Lett.*, *37*, L06602, doi:10.1029/2010GL042372.

Willis, J. K., and L.-L. Fu (2008), Combining altimeter and subsurface float data to estimate the time-averaged circulation in the upper ocean, *J. Geophys. Res.*, *113*, C12017, doi:10.1029/2007JC004690.

Wu, Z., and N. E. Huang (2009), Ensemble empirical mode decomposition: A noise-assisted data analysis method, *Adv. Adaptive Data Anal.*, *1*(1), 1–41, doi:10.1142/S1793536909000047.

Xu, X., W. J. Schmitz Jr., H. E. Hurlburt, P. J. Hogan, and E. P. Chassignet (2010), Transport of Nordic Seas overflow water into and within the Irminger Sea: An eddy-resolving simulation and observations, *J. Geophys. Res.*, *115*, C12048, doi:10.1029/2010JC006351.

Xu, X., W. J. Schmitz Jr., H. E. Hurlburt, and P. J. Hogan (2012), Mean Atlantic meridional overturning circulation across 26.5°N from eddy-resolving simulations compared to observations, *J. Geophys. Res.*, *117*, C03042, doi:10.1029/2010JC007586.

Xu, X., H. E. Hurlburt, W. J. Schmitz Jr., R. J. Zantopp, J. Fischer, and P. J. Hogan (2013), On the currents and transports connected with the Atlantic meridional overturning circulation in the subpolar North Atlantic, *J. Geophys. Res. Oceans*, *118*, 502–516, doi:10.1002/jgrc.20065.

Zhang, R. (2010), Latitudinal dependence of Atlantic meridional overturning circulation (AMOC) variations, *Geophys. Res. Lett.*, *37*, L16703, doi:10.1029/2010GL044474.

Zhao, J., and W. E. Johns (2014a), Wind driven seasonal cycle of the Atlantic meridional overturning circulation, *J. Phys. Oceanogr.*, *44*(6), 1541–1562, doi:10.1175/JPO-D-13-0144.1.

Zhao, J., and W. E. Johns (2014b), Wind-forced interannual variability of the Atlantic meridional overturning circulation at 26.5°N, *J. Geophys. Res. Oceans*, *119*, 2403–2419, doi:10.1002/2013JC009407.